IEEE Access
Multidisciplinary | Rapid Review | Open Access Journal

Received 18 July 2023, accepted 1 August 2023, date of publication 7 August 2023, date of current version 14 August 2023.

Digital Object Identifier 10.1109/ACCESS.2023.3302402

RESEARCH ARTICLE

SalCor: A Hierarchical Saliency-Driven Segmentation Model With Local Correntropy for Medical Images

ADITI JOSHI[1], MOHAMMED SAQUIB KHAN[2], (Member, IEEE), JIN KIM[3], AND KWANG NAM CHOI[1]

[1]Department of Computer Science and Engineering, Chung-Ang University, Seoul 06974, South Korea
[2]Beyond 5G Team, Samsung Research and Development Institute, Bengaluru 560037, India
[3]SecuLayer Inc., Seoul 04784, South Korea

Corresponding author: Kwang Nam Choi (knchoi@cau.ac.kr)

This work was supported in part by the Chung-Ang University Young Scientist Scholarship, in 2021; and in part by the Institute of Information and Communications Technology Planning and Evaluation (IITP) Grant Funded by the Korean Government [Ministry of Science, Information and Communication Technology (MSIT)], Development of the Technology to Automate the Recommendations for Big Data Analytic Models that Define Data Characteristics and Problems, under Grant 2020-0-00107.

ABSTRACT In image segmentation, noise and nonuniform intensity can lead to performance degradation in existing models, particularly when dealing with shadow artifacts. This study proposes a hierarchical saliency-driven segmentation model with local correntropy (SalCor) to address this problem, incorporating saliency information with local correntropy-based K-means clustering to formulate an energy function. This approach enables it to extract objects with complex backgrounds effectively regardless of noise and intensity inhomogeneity. An adaptive weight function is introduced to dynamically adjust the intensities of the energy functions (external and internal) based on the image information, resulting in enhanced model resilience to contour initialization and improved robustness. The SalCor model can handle noise robustly by leveraging the local correntropy-based K-means clustering. The proposed approach is evaluated on synthetic and real images, including medical images, such as brain and mammogram magnetic resonance imaging (MRI) and coronavirus disease 2019 (COVID-19) computed tomography images, and is compared with state-of-the-art models. The statistical analysis confirms the SalCor model's exceptional precision and efficiency. These outcomes indicate that SalCor holds great potential for detecting brain tumors and mammogram tumors in MRIs and early diagnosis of COVID-19.

INDEX TERMS Active contours, brain magnetic resonance imaging (MRI), coronavirus disease 2019 (COVID-19), image segmentation, level set, mammogram, medical image, saliency.

I. INTRODUCTION

IMAGE segmentation is a fundamental component in most image processing and computer vision tasks, with such applications as object recognition and tracking, medical imaging, face recognition, autonomous driving and robotics, pedestrian detection, and augmented and virtual reality [1]. However, image segmentation accuracy is significantly affected by intensity inhomogeneity and noise in observed images, which can spread inaccuracies across the complete image analysis process. Therefore, techniques to overcome these limitations to ensure the reliability and accuracy of the segmentation model are highly desirable.

The literature contains a numerous image segmentation algorithms encompassing various stages of development. These include initial methodologies like thresholding, histogram-based clustering, region-growing, K-means clustering, and watersheds, as well as more sophisticated approaches like active contours, conditional and Markov random fields, sparsity-based, and graph cuts methods. While

The associate editor coordinating the review of this manuscript and approving it for publication was Kumaradevan Punithakumar.

deep learning models offer greater precision compared to alternative methods, they need more extensive datasets and increased computational resources [2]. Thus, the active contour model (ACM) based on deformable contours has gained attention in recent years.

The ACMs, also known as snakes, are mathematical models for image segmentation and object recognition. The idea behind an ACM is to use a deformable curve or surface attracted to the edges of objects of interest in an image. An ACM can determine the object boundary and segment it from the rest of the image by iteratively adjusting the shape of the curve or surface based on the image features. Moreover, ACMs have been widely studied and developed over the past few decades, and several categories of ACMs exist, including parametric and nonparametric models [3], edge-based models [4], [5], [6], [7], region-based models [8], [9], [10], [11], [12], [13], [14], and hybrid models [15], [16], [17], [18], [19], [20]. Parametric models, such as the original snake proposed by Kass et al. [3], use a predefined shape and can be computationally efficient but may not be flexible enough to capture complex shapes. Nonparametric models do not make any assumptions about the shape of objects and can be more flexible but may be computationally expensive. As the name implies, edge-based models focus on detecting and linking edges in an image to identify object boundaries effectively but can struggle with noise and may miss objects with unclear edges. Region-based models, which consider the interior and edge of an object, are helpful for objects with varying intensity levels or those in noisy images. However, they can be sensitive to the initial conditions and may not work well on objects with unclear boundaries. Hybrid models combine approaches to leverage their strengths and minimize their weaknesses but can be challenging to implement and optimize. Ultimately, the choice of segmentation model depends on the specific application and image characteristics, and a combination of models may be necessary to achieve the best results.

Li et al. proposed popular edge-based methods for level-set segmentation, including level-set evolution without reinitialization [5] and distance-regularized level set [6], which do not require reinitialization. However, these methods may not perform well on weak boundaries. While region-based models were initially developed for objects with uniform intensity, such as the Chan–Vese model [9], they may be unsuitable for images with an nonuniform intensity or texture.

Local region-based models have been developed to address this problem, such as local binary fitting (LBF) [10], where the region scalable fitting energy is used to capture nonuniform intensity images, adapting intensity information locally using a Gaussian kernel. The local correntropy-based K-means clustering model uses K-means clustering with the pixel-to-cluster distance to reduce noise influence on image segmentation [13]. Nevertheless, it is sensitive to initialization, and its iterative approach delays the final segmentation results.

Other methods, such as the variational level-set approach for bias correction and segmentation (VLSBCS) [11] and local statistical ACM (LSACM) [14], use a bias field correction term in their formulations to improve the segmentation of nonuniform intensity images. These methods approximate the nonuniform intensity map of the entire image and operate in the context of local energy. However, severe noise and distinct nonuniform intensity factors can impede effective and accurate image segmentation in local ACMs. Thus, a local/global region-based ACM was proposed in [12] that integrates a global signed pressure force function using intensity means from [9]. However, two drawbacks of these ACMs are the struggle of the evolving contour to conform to image topology changes and the high sensitivity to the initial conditions. The configuration of parameters at the beginning and the initial shape of the contour (seeds) are required for these ACMs, which can be challenging and require technical expertise from end users.

In recent decades, medical imaging has become a prominent area of application for image processing and segmentation [21]. Medical image segmentation is a critical component in medical image analysis, as it allows for the precise identification and extraction of anatomical structures or regions of interest (ROIs) from medical images. This information is crucial in various clinical applications, including diagnosis, treatment planning, and disease monitoring [22]. For instance, accurate segmentation of medical images, including computed tomography (CT) scans or magnetic resonance imaging (MRI), can help identify tumor boundaries, brain lesions, coronavirus disease 2019 (COVID-19) infection in the lungs, and abnormalities in other organs. Brain MRI and CT scans of COVID-19-infected lungs are among the most common radiological imaging techniques that function as a workable strategy for the timely identification and evaluation of these diseases [23].

Segmentation of brain tumors from MRIs and COVID-19 infections from lung CT scans are considered some of the most complex and challenging tasks in medical imaging [24], [25]. First, brain MRI and lung CT images have complex structures and textures, making it difficult to differentiate between healthy tissue and tumors or infections. Second, the boundaries between the tissue of interest and the surrounding tissue are not always clear, making it challenging to define a clear boundary for the active contour to follow. Third, the pixels intensity values within the ROIs and surrounding tissue may overlap, making it difficult to distinguish between them using only intensity-based information. Finally, the size, shape, and location of tumors and infected regions in different patients can vary considerably, making it challenging to design a generic model that works well for all cases.

Currently, in medicine, identifying and categorizing brain tumors from multiple MRIs and COVID-19 infections from multiple CT scans necessitates manual intervention. However, this process is time-consuming and demanding, requiring highly experienced and well-trained radiologists to

perform the task accurately. Thus, these challenges require sophisticated algorithms that can handle the complex nature of these medical images to improve the precision and robustness of the segmentation process. As far as the authors are aware, no previous attempt has been made to create an ACM capable of segmenting brain tumors from MRIs and detecting COVID-19 in CT scans. Hence, the objective of this research is to create an ACM that can perform accurate and efficient segmentation on various image types, including those suffering from nonuniform intensity, low contrast, and noise, in synthetic and real images and medical imaging applications.

Recently, saliency-based approaches have become increasingly popular for identifying essential parts of an image in image segmentation. This approach is applied in computer vision applications and can reduce computational burden by focusing on the most relevant parts of the image. Various techniques for measuring and analyzing saliency have been developed, which achieved state-of-the-art (SOTA) results [26], [27], [28], [29], [30]. For instance, a saliency-driven approach for color image segmentation was proposed in [26], constructing a facial saliency map to segment and track faces. The authors of [27] proposed the saliency-SVM (support vector machine) model that uses saliency and addresses image segmentation as a binary classification task. In [28], the affinity propagation clustering algorithm was employed to merge regional saliency with the random walk method for segmentation. Besides, the authors suggest using visual saliency with ACMs to improve the segmentation outcomes in [29]. Thus, saliency-based segmentation is a promising approach for improving image analysis and is likely to be an active area of research and development in the future.

The mentioned saliency-based ACMs can effectively segment images with clear boundaries and intensity uniformity; however, they are inadequate for segmenting images with distorted or nonuniform intensity distributions, such as real and medical images. In addition, some ACMs are susceptible to initialization and noise. Therefore, a novel hierarchical saliency-driven segmentation model with local correntropy (SalCor) is proposed to address the challenges associated with image segmentation for different initializations in the presence of nonuniform intensity and noise.

The significant contributions were made in this study and can be succinctly summarized as

- A novel SalCor model is proposed to address the challenges of severe nonuniform intensity and noise in image segmentation. This model employs a novel energy function incorporating saliency and color variance information in the level set. Thus, it can effectively extract objects with complex backgrounds irrespective of nonuniform intensity and noise.
- An adaptive weighted function is introduced using local and global image dissimilarities. This design enhances model resilience to contour initialization and improves its robustness.
- The SalCor model is made robust against noise by leveraging K-means clustering based on local correntropy with the exponential family (LCE) function.
- The SalCor model with Riemannian steepest descent (RSD) improves the image segmentation speed and accuracy over conventional gradient descent (SGD).
- Finally, contour evolutions on various images confirm the effectiveness and advantages of the SalCor model over SOTA models.

The paper is structured as follows. Section II presents the SalCor model using saliency and color intensity variance, including the mathematical model for the evolution of the initial contour. Section III presents simulation results and compares the SalCor model with SOTA methods using synthetic and real images. Section IV performs quantitative and qualitative analyses on multiple medical and real image datasets. Discussion is done in Section V. Finally, Section VI concludes the paper.

II. PROPOSED SalCor MODEL

The proposed SalCor model is presented in this section to address the problems posed by significant nonuniform intensity and noise in images. A novel energy function is formulated to extract objects efficiently, even with complex backgrounds and high noise levels. Furthermore, a novel level-set evolution approach is proposed in the SalCor model that employs internal and external energy functions. This design enhances model robustness to initialization and allows it to converge faster than other segmentation models.

The proposed energy function E_{SalCor} is defined in (1) for an input image $I : \Omega \rightarrow \Re^2$ and a level-set function ϕ with an initial contour $C : x \in \Omega | \phi = 0$ in an image domain Ω. We let $\Omega_0 : x \in \Omega | \phi = 0$ be the zero level- set, and $\Omega_{\text{in}} : \Omega | \phi < 0$ and $\Omega_{\text{ex}} : \Omega | \phi > 0$ be the domains inside and outside of Ω_0, respectively.:

$$E_{\text{SalCor}} = E_{\text{ex}}(\phi) + E_{\text{in}}(\phi). \tag{1}$$

In (1), the external energy function E_{ex} is computed based on gradient, region, and saliency information, whereas the internal energy function E_{in} is based on LCE and acts as a constraint to guide the level-set evolution.

When dealing with images that exhibit nonuniform intensity and color variation, the pixels tend to cluster, causing pixels with comparable intensity and saliency to be given to Ω_{in} and Ω_{ex}. To address this problem, the proposed external energy function E_{ex} considers the saliency information and color intensity variance for Ω_{in} and Ω_{ex} of I:

$$E_{\text{ex}}(\phi) = \underbrace{\alpha \left[\int_{\Omega} hH_{\varepsilon}(\phi) Y_{\text{in}}(x)dx + \int_{\Omega} h(1 - H_{\varepsilon}(\phi)) Y_{\text{ex}}(x)dx \right]}_{(2.1)}$$

$$+\lambda_1 \underbrace{\left[\int_\Omega hH_\varepsilon(\phi)\, Z_{\text{in}}(x)dx + \int_\Omega h\,(1-H_\varepsilon(\phi))\, Z_{\text{ex}}(x)dx\right]}_{(2.2)}, \tag{2}$$

where

$$Y_{\text{in}}(x) = [S(x) - s_1]^2,\ Y_{\text{ex}}(x) = [S(x) - s_2]^2, \tag{3}$$

$$Z_{\text{in}}(x) = |I(x) - c_1|^2 + |I(x) - f|^2,$$

$$Z_{\text{ex}}(x) = |I(x) - c_2|^2, \tag{4}$$

where $H_\varepsilon(\phi)$ denotes the $\varepsilon-$Heaviside function in (2) with $\varepsilon \geq 0$. The scaling constants α and λ_1 are fixed and positive, and correspond to the saliency information (2.1) and color intensity variance (2.2) in (2), respectively. In addition, an edge indicator h is used for both (2.1) and (2.2):

$$h = \frac{1}{1 + \left|\nabla \kappa_\rho * I\right|^2}, \tag{5}$$

where

$$\kappa_\rho(x, y) = \frac{1}{2\pi\rho^2} e^{\frac{-x^2+y^2}{2\rho^2}}, \tag{6}$$

∇, and $*$ represent the Gaussian kernel with standard deviation ρ, the gradient operator, and the convolution operator, respectively.

The identification of the most prominent objects or regions in an image, such as edges, colors, and textures, is the aim of saliency information S in (3) and is given as [31]:

$$S(x) = \left|\bar{I}(x) - I_\kappa(x)\right|, \tag{7}$$

where the mean pixel value of I is represented by $\bar{I}$ and the blurred image I_κ is obtained by convolving the original image I with a Gaussian filter κ_ρ. In addition, the saliency means for the regions Ω_{in} and Ω_{ex} are respectively denoted by s_1 and s_2:

$$s_1 = \frac{\int_\Omega S(x) \cdot H_\varepsilon(\phi)\, dx}{\int_\Omega H_\varepsilon(\phi)\, dx},\ s_2 = \frac{\int_\Omega S(x) \cdot (1 - H_\varepsilon(\phi))\, dx}{\int_\Omega (1 - H_\varepsilon(\phi))\, dx}. \tag{8}$$

In (4), the scalar approximations of mean intensities for the regions Ω_{in} and Ω_{ex} are denoted by c_1 and c_2, respectively. In addition, the median scalar approximation for the region Ω_{in} is represented by f:

$$\begin{aligned} c_1 &= \text{mean}\,(I(x) \in \Omega_{\text{in}}) \cdot \omega, \\ c_2 &= \text{mean}\,(I(x) \in \Omega_{\text{ex}}) \cdot \omega, \\ f &= \text{median}\,(I(x) \in \Omega_{\text{in}}) \cdot \omega. \end{aligned} \tag{9}$$

To increase the resilience of the SalCor model towards initialization, an adaptive weighted function is introduced and applied to c_1, c_2, and f:

$$\omega = \int_\Omega \|Z_{\text{in}}(x)\|_2 H_\varepsilon(\phi)\, dx + \int_\Omega \|Z_{\text{ex}}(x)\|_2 (1 - H_\varepsilon(\phi))\, dx, \tag{10}$$

where $\|\cdot\|$ is the L2 norm. Compared to mean values, median values are more proximate to the edge of an object in terms of pixel values. This characteristic makes the median value effective in reducing noise and preserving fine details like thin lines.

Using the external energy function alone for segmentation can lead to inaccuracies and irregularities, resulting in the appearance of false contours or singularities. The LCE function for the local region overcomes this limitation, helping to address nonuniform intensity and low contrast. The Correntropy-based clustering in LCE ensures adaptive weighting of objects, making it robust to outliers. It is defined as follows

$$\begin{aligned} &E_{\text{in}}(\phi) \\ &= -\lambda_2 \int_\Omega \int_\Omega \kappa_\rho \omega \log\left[J\left(I(x, y)\,|c_1\right)\right] H_\varepsilon(\phi)\, dydx \\ &\quad - \lambda_3 \int_\Omega \int_\Omega \kappa_\rho \omega \log\left[J\left(I(x, y)\,|c_2\right)\right] (1 - H_\varepsilon(\phi))\, dydx \\ &\quad - \varepsilon \int_\Omega \log\left[J(\phi)\right] dx \end{aligned} \tag{11}$$

where $\lambda_2, \lambda_3 \geq 0$ are predefined constants, and J is one of the exponential family functions. The exponential family comprises various distributions such as Gaussian, Poisson, Bernoulli, and Rayleigh, which have been extensively used to model the noise structure in several image acquisition devices. For instance, Poisson distribution helps model noise in charge-coupled device cameras or X-ray images, whereas Rayleigh distribution is appropriate for ultrasound images [32].

Therefore, E_{SalCor} proposed in (1) can be expressed as:

$$\begin{aligned} &E_{\text{SalCor}}(\phi) \\ &= \alpha \left[\int_\Omega hH_\varepsilon(\phi)\, Y_{\text{in}}(x)dx + \int_\Omega h\,(1 - H_\varepsilon(\phi))\, Y_{\text{ex}}(x)dx\right] \\ &\quad + \lambda_1 \left[\int_\Omega hH_\varepsilon(\phi)\, Z_{\text{in}}(x)dx + \int_\Omega h\,(1 - H_\varepsilon(\phi))\, Z_{\text{ex}}(x)dx\right] \\ &\quad - \lambda_2 \int_\Omega \int_\Omega \kappa_\rho \omega \log\left[J\left(I(x, y)\,|c_1\right)\right] H_\varepsilon(\phi)\, dydx \\ &\quad - \lambda_3 \int_\Omega \int_\Omega \kappa_\rho \omega \log\left[J\left(I(x, y)\,|c_2\right)\right] (1 - H_\varepsilon(\phi))\, dydx \\ &\quad - \varepsilon \int_\Omega \log\left[J(\phi)\right] dx \end{aligned} \tag{12}$$

Next, minimize (12) by taking its derivative using the calculus of variations as

$$\begin{aligned}\frac{\partial E_{\text{SalCor}}}{\partial \phi} &= \alpha\left[hY_{\text{in}}(x) - hY_{\text{ex}}(x)\right] \\ &+ \lambda_1\left[hZ_{\text{in}}(x) - hZ_{\text{ex}}(x)\right] \\ &+ \kappa_\rho * \omega\left[\lambda_2 \log\left[J\left(I(x,y)|\, c_1\right)\right] - \lambda_3 \log\left[J\left(I(x,y)|\, c_2\right)\right]\right] \\ &+ 2\varepsilon\,|\phi| \end{aligned} \tag{13}$$

The SGD ensures that ACMs converge. Although they are prone to local minima, numerous iterations are required, increasing the runtime. Thus, the RSD method was proposed to enhance segmentation accuracy and decrease runtime [33]. The evolution of ϕ concerning time t in (13) can be

$$\begin{aligned}\frac{\partial \phi}{\partial t} &= \frac{\partial E_{\text{SalCor}}}{\partial \phi} \\ &= \phi + \alpha h\left[Y_{\text{in}}(x) - Y_{\text{ex}}(x)\right] + \lambda_1 h\left[Z_{\text{in}}(x) - Z_{\text{ex}}(x)\right] \\ &\quad + \mathcal{N}^{-1}(\phi)\,\nabla E_{\text{in}}(I;\phi) \end{aligned} \tag{14}$$

where

$$\begin{aligned}&\nabla E_{\text{in}}(I;\phi) \\ &= \kappa_\rho * \omega\left[\lambda_2 \log\left[J\left(I(x,y)|\, c_1\right)\right] - \lambda_3 \log\left[J\left(I(x,y)|\, c_2\right)\right]\right] \\ &\quad + 2\varepsilon\,|\phi|\,, \end{aligned} \tag{15}$$

$$\begin{aligned}&\mathcal{N}(\phi) \\ &= \kappa_\rho * \begin{cases} |\delta_\varepsilon(\phi)|\, B_J\left[c_2 \| c_1\right], & \phi > 0 \\ |\delta_\varepsilon(\phi)|\, B_J\left[c_1 \| c_2\right], & \phi < 0 \end{cases} \end{aligned} \tag{16}$$

is the RSD, $\delta_\varepsilon = \varepsilon/\pi\left(\phi^2 + \varepsilon^2\right)$ is the Dirac Delta function, and B_J is the J-Bregman divergence [34]. In (14), the matrix inversion, $\mathcal{N}^{-1}(\phi)$, can be easily performed because $\mathcal{N}(\phi)$ is a positive diagonal matrix. The $\mathcal{N}$ is derived using *Definition 1* in *Theorem 1*.

Definition 1: [35] The distribution family of a random variable $\mathrm{S}\left\{F_{\boldsymbol{\eta}} : \boldsymbol{\eta} \in \Im \subseteq \mathbb{R}_c\right\}$ is classified as a c-parameter canonical exponential family when certain conditions are met. Specifically, the natural parameter vector $\boldsymbol{\eta} = (\eta_1, \ldots, \eta_c) \in \mathbb{R}$, and the log-normalizer $A(\boldsymbol{\eta})$ exists within a natural parameter space $\Im = \{\boldsymbol{\eta} \in \mathbb{R}_c; -\infty < A(\boldsymbol{\eta}) < \infty\}$. The probability density function of $F_{\boldsymbol{\eta}}$ can be expressed as (17), where $D(s)$ denotes the reference density, $\mathbf{T} = (T_1, \ldots, T_c)^{\mathrm{T}}$ is the natural sufficient statistic, and $\langle\cdot\rangle$ denotes the scalar product.

$$f(s|\boldsymbol{\eta}) = D(s)\exp\left[\left\langle \boldsymbol{\eta}^{\mathrm{T}}, \mathbf{T}(s)\right\rangle - A(\boldsymbol{\eta})\right] \tag{17}$$

Theorem 1: Assuming (17) in *Definition 1* is satisfied, then $\mathcal{N}(\phi)$ can be represented as a diagonal matrix whose elements are given by:

$$\mathcal{N}(\phi) = \begin{cases} \int\limits_{\Omega} \kappa_\rho\, |\delta_\varepsilon(\phi)|\, B_J\left[c_2 \| c_1\right] dx, & \phi > 0 \\ \int\limits_{\Omega} \kappa_\rho\, |\delta_\varepsilon(\phi)|\, B_J\left[c_1 \| c_2\right] dx, & \phi < 0 \end{cases} \tag{18}$$

where

$$\begin{aligned}B_J\left[c_2 \| c_1\right] &\triangleq A\left(\boldsymbol{\eta}_{c_2}\right) - A\left(\boldsymbol{\eta}_{c_1}\right) \\ &\quad - \left\langle A\left(\boldsymbol{\eta}_{c_2} - \boldsymbol{\eta}_{c_1}\right), \nabla_{\boldsymbol{\eta}_{c_1}} A\left(\boldsymbol{\eta}_{c_1}\right)\right\rangle, \end{aligned} \tag{19}$$

and the gradient of $A(\boldsymbol{\eta})$ is denoted as $\nabla_{\boldsymbol{\eta}} A(\boldsymbol{\eta})$. By employing convolution, (18) can be expressed as (16). It can be concluded that $\mathcal{N}(\phi)$ is positive only when $\delta_\varepsilon(\phi)$ does not approach zero.

Proof: Let the Fisher Information Matrix (FIM) be written as [36]

$$\mathcal{N}(\phi) \triangleq \mathbb{E}\left[\frac{\partial^2}{\partial \phi_x \partial \phi_y} \log\left[J\left(I|\phi\right)\right]\right], \tag{20}$$

where $\mathbb{E}$ denotes the expectation and

$$J(I|\phi) = \int\limits_{\{\Omega:\phi>0\}} J(I|c_1)\, dx + \int\limits_{\{\Omega:\phi<0\}} J(I|c_2)\, dx.$$

Now, the derivatives of the FIM is expressed as

$$\begin{aligned}\mathcal{N}(\phi) &= -\delta_\varepsilon(\phi)\,\mathbb{E}\left[\log\left(J\left(I|c_1\right)|\phi\right)\right] \\ &\quad - \delta_\varepsilon(-\phi)\,\mathbb{E}\left[\log\left(J\left(I|c_2\right)|\phi\right)\right]. \end{aligned} \tag{21}$$

Applying Gaussian kernel in (6) on (21), (21) becomes

$$\mathcal{N}(\phi) = \kappa_\rho(x,y) * \left\{\begin{array}{c} -\delta_\varepsilon(\phi)\,\mathbb{E}\left[\log\left(J\left(I|c_1\right)|\phi\right)\right] \\ -\delta_\varepsilon(-\phi)\,\mathbb{E}\left[\log\left(J\left(I|c_2\right)|\phi\right)\right] \end{array}\right\}. \tag{22}$$

Since $\delta(-\phi) = -\delta(\phi)$, (22) can be expressed as

$$\mathcal{N}(\phi) = \kappa_\rho(x,y) * \left\{-\delta_\varepsilon(\phi)\,\mathbb{E}\left[\log\left(\frac{J\left(I|c_1\right)}{J\left(I|c_2\right)}\right)\middle|\,\phi\right]\right\}. \tag{23}$$

With Kullback-Leibler divergences [34],

$$\mathcal{N}(\phi) = \kappa_\rho(x,y) * \begin{cases} |\delta_\varepsilon(\phi)|\, KL_J\left(c_1 \| c_2\right), & \phi(x) > 0 \\ |\delta_\varepsilon(\phi)|\, KL_J\left(c_2 \| c_1\right), & \phi(x) < 0 \end{cases} \tag{24}$$

Finally, (24) can be reformulated using the Bregman divergence, as given in (16). ■

According to [33], preconditioning $\nabla E_{\text{in}}(I;\phi)$ with $\mathcal{N}^{-1}(\phi)$ in (14) results in isotropic convergence properties around the local minima, regardless of the model parametrization or signal dependencies. Fig. 1 illustrates that the RSD converges faster than the simple SGD. Specifically, the RSD converged after the fourth iteration, whereas the SGD required ten iterations.

The SalCor model derives region information (global features), including color intensity variance and saliency, from I. This approach allows for a high degree of flexibility in initializing ϕ and can be initialized as follows

$$\phi_{t=0} = p, x \in \Omega, \tag{25}$$

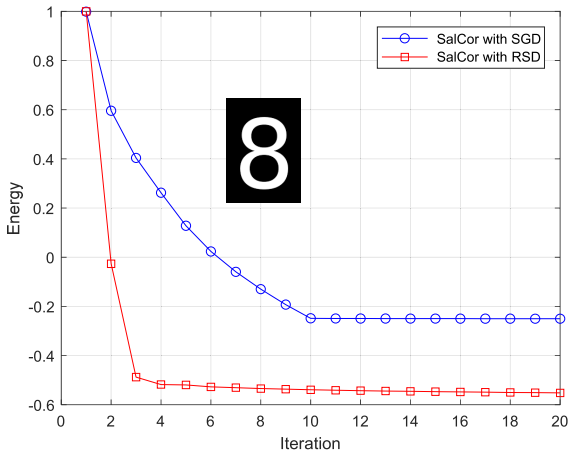

FIGURE 1. The energy convergence of SalCor with RSD and SGD.

where $p \geq 0$ is a constant initialization parameter. A threshold γ must be implemented to halt the process to ensure the proper evolution of ϕ, as follows:

$$\left|\frac{\partial \phi}{\partial t}\Delta t\right| = |\phi_{t+1} - \phi_t| < \gamma, \tag{26}$$

because ϕ will no longer converges. In (26), Δt denotes the time interval parameter. The algorithmic steps of the SalCor model are outlined in **Algorithm 1**.

Algorithm 1 The Proposed SalCor Model

Input: $I, \alpha, \lambda_1, \lambda_2, \lambda_3, \varepsilon$ and γ

1: **Initialization:** ϕ_0 by (25) and $\omega = 1$
2: **for** 1 to maximum iterations **do**
3: Compute h using (5)
4: Compute $S(x)$ using (7)
5: Compute s_1 and s_2 by (8) and c_1, c_2, and f by (9)
6: Update adaptive weight ω using (10)
7: Compute $\mathcal{N}$ using (16)
8: Obtain the final segmentation using (14)
9: **if** (26) is satisfied **then**
10: Jump to Step 3
11: **else**
12: Stop evolution
13: **end if**
14: **end for**

Output: Final ϕ

III. SIMULATIONS AND RESULTS

The MATLAB implementation of the SalCor model was executed on a computer system equipped with an Intel Core i7 processor clocked at 3.60 GHz with 8 GB RAM. Both synthetic and real images were tested to evaluate the SalCor model and compare its performance with other SOTA models, such as CV [9], LBF [10], VLSBCS [11], LSACM [14], LGFI [37], and McGKFCM [38]. To set the optimal values for parameters α, λ_1, λ_2, λ_3, ε, and ρ, experiments on an image

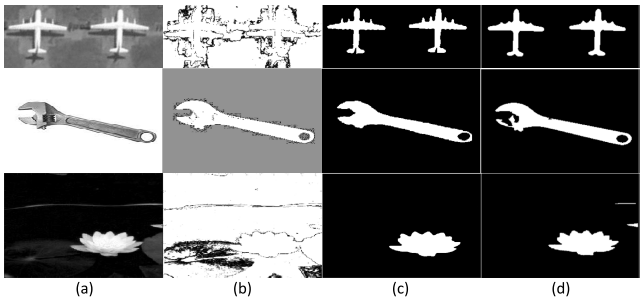

FIGURE 2. Effect of Saliency on image segmentation. (a) Original image, (b) saliency information, (c) result with saliency, and (d) result without saliency.

from mini-MIAS dataset [39] is performed. The Accuracy of the segmentation is calculated for different combinations of three different values of α, λ_1, λ_2, λ_3, ε, and ρ as

$$\text{Accuracy}_{GT} = \frac{|R_S \cap R_{GT}|}{|R_S \cup R_{GT}|} \tag{27}$$

where R_S and R_{GT} denote the segmented region and ground truth, respectively. Table 1 presents the accuracy achieved by different combinations of parameters. It is important to note that the accuracy for different values of λ_2 and λ_3 are not included in the table. This omission is due to the observed instability in contour evolution during the initial iterations when $\lambda_1, \lambda_2 > 6$, caused by an oversaturation of energies. Consequently, the values of λ_2 and λ_3 have been selected as 1 since this selection consistently yields the best accuracy. From the experiment, it was observed that the accuracy is almost same for $\rho > 0.5$ and the algorithm's complexity is determined by the value of ρ. A smaller ρ reduces complexity, while increasing ρ enlarges the smoothing kernel's window size, resulting in higher computational demands and increased time complexity. Therefore, the SalCor model used fixed parameters for further experiments, which are listed in Table 2. On the other hand, parameters for the other models were retrieved from their corresponding literature.

Fig. 2 illustrates the segmentation obtained using the SalCor model, showcasing the impact of incorporating saliency information into the level-set function. The input image used in the experiment is a combination of synthetic and real images as shown in Fig. 2(a). Fig. 2(b) shows the saliency obtained using the SalCor model. The segmentation result of the SalCor model using the saliency information is depicted in Fig. 2(c), whereas the segmentation without saliency is obtained by initializing α to zero and is presented in Fig. 2(d). The incorporation of saliency information improves the reliability and accuracy of the SalCor model, as demonstrated by the segmentation outcomes.

Fig. 3 shows a comparison of the segmentation outcomes from all previous SOTA methods and the SalCor model for an image with intensity variation. The image in the comparison initially have uniform intensity (Fig. 3(a): Row 1) but has altered intensity distributions to some extent (Fig. 3(a): Rows 2, 3, and 4), making it challenging to segment even

TABLE 1. The effect of α, λ_1, ε, and ρ on the segmentation performance of SalCor with Accuracy metric.

α	0.01								0.05							
λ_1	0.1				0.5				0.1				0.5			
ε	1		1.4		1		1.4		1		1.4		1		1.4	
ρ	0.5	0.7	0.5	0.7	0.5	0.7	0.5	0.7	0.5	0.7	0.5	0.7	0.5	0.7	0.5	0.7
Accuracy	0.955	0.957	0.959	0.961	0.958	0.962	0.956	0.963	0.964	0.977	0.975	0.981	0.966	0.962	0.967	0.969

TABLE 2. Parameters of the SalCor model.

Parameter	Symbol	Value
Saliency scaling constant	α	0.05
Color intensity variance constant	λ_1	0.1
Force term scaling constants	λ_2, λ_3	1
Constant epsilon	ε	1.4
Standard deviation	ρ	0.7
Stopping Threshold	γ	$N \times 0.005$
Constant for initial level set	p	1
Time step	Δt	1

*N is the number of pixels in I.

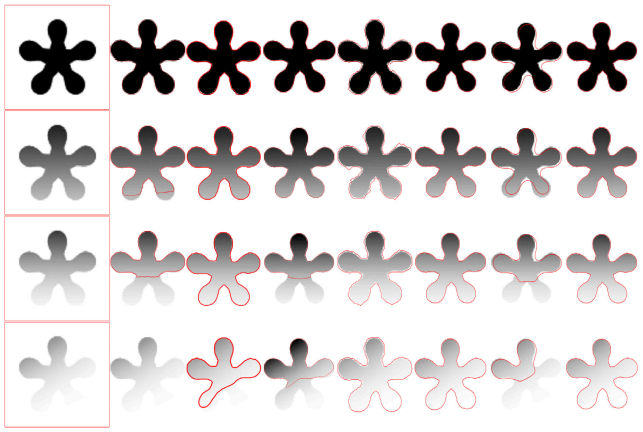

FIGURE 3. Image Segmentation with intensity variation. (a) Original image, (b) CV, (c) LBF, (d) VLSBCS, (e) LSACM, (f) LGFI, (g) McGKFCM, and (h) proposed SalCor.

manually. Fig. 3(a) shows the input images with initial contours, and Fig. 3(b)-(h) show the segmentation outcomes extracted using the CV, LBF, VLSBCS, LGFI, McGKFCM, and SalCor models, respectively. The results reveal that the SalCor and LGFI models provide the most accurate segmentation, irrespective of nonuniform intensity. In addition, the LSACM model fails to determine the precise object edge, whereas the CV, LBF, and VLSBCS models provide relatively precise segmentation for the uniform intensity image (Row 1), but their performance deteriorates with increased nonuniform intensity. The McGKFCM model fails to detect precise object boundaries, even for the uniform intensity image.

Most SOTA ACMs require an accurate level-set initialization and exhibit sensitivity to position of contour initialization. In contrast, the SalCor model is exceptionally robust to the position of the initial contour and consistently produces the identical results regardless of the contour position. This property of the proposed model is demonstrated in Fig. 4, where a synthetic image with severe

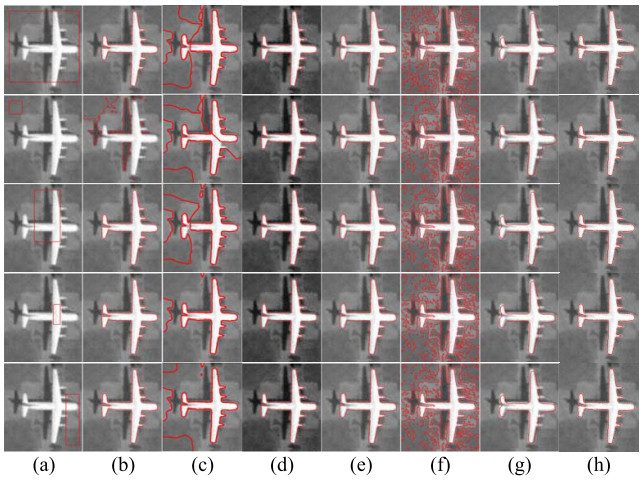

FIGURE 4. Effect of initial contour position on proposed SalCor model. (a) Original image, (b) CV, (c) LBF, (d) VLSBCS, (e) LSACM, (f) LGFI, (g) McGKFCM, and (h) proposed SalCor.

nonuniform intensity is used. Fig. 4(a) exhibit distinct initial contours, while Fig. 4(b)-(h) show the segmentation outcomes obtained using the CV, LBF, VLSBCS, LGFI, McGKFCM, and SalCor models, respectively. The results demonstrate that SalCor, VLSBCS and LSACM exhibit effective performance in dealing with different initial contour positions on images with nonuniform intensity and noise conditions. Notably, the SalCor model achieved precise segmentation even when the object edges were blurred, proving its robustness against severe intensity variation and initialization. Thus, this paper used a constant initialized contour for all images.

Fig. 5 illustrates the ability of the SalCor model to address noise in input images. Two types of noise, Gaussian and salt-and-pepper, are present in the two images being used. In Columns 1 to 4, the level of Gaussian noise increased from 0.01 to 0.04, whereas in Columns 5 to 8, the level of salt-and-pepper noise increased from 0.01 to 0.04. All the models except McGKFCM produce false contours around the ROI edges due to their inability to eliminate noise from the images. Although the McGKFCM model performs well, the segmentation accuracy is not as close to the SalCor model. In contrast, the SalCor model leverages saliency information to accurately identify the ROI while distinguishing it from the surrounding background, while utilizing LCE to eliminate most of the noise. As a result, the SalCor model is robust to noise, enabling it to accurately segment the ROI despite variations in image complexity and noise type.

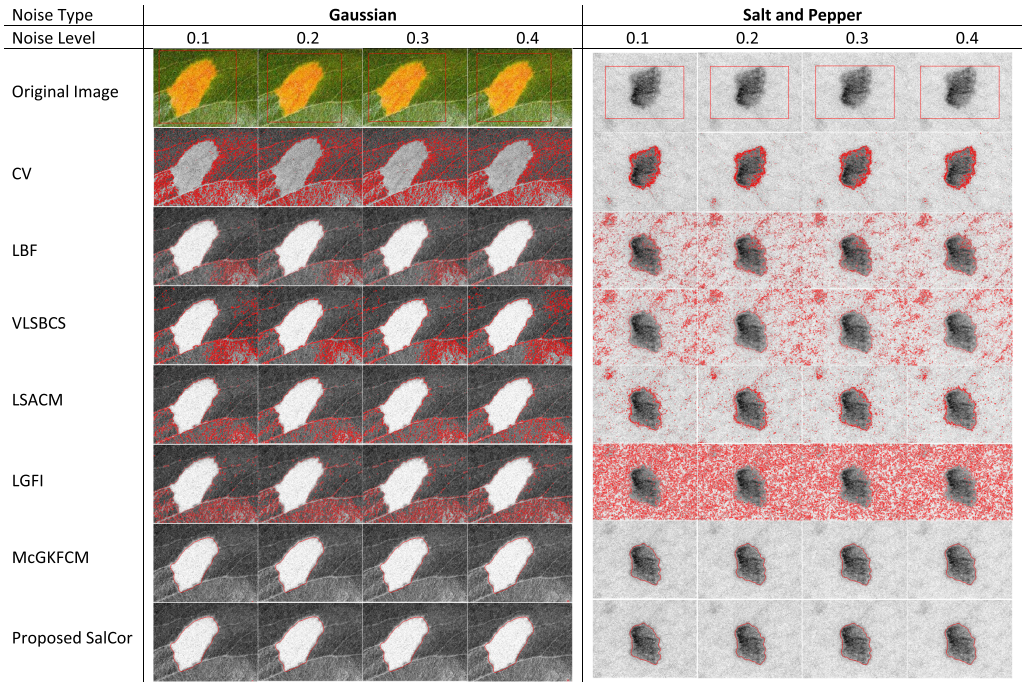

FIGURE 5. Segmentation and corresponding comparisons of images with varying levels of Gaussian noise and Salt and Pepper noise: (0.01, 0.02, 0.03, 0.04).

Fig. 6 depicts the performance evaluation of the SalCor model and SOTA models using uniform and nonuniform intensity synthetic and real images. The original images are presented in Row 1, whereas Rows 2 to 8 show the segmentation results of various models, including CV, LBF, VLSBCS, LSACM, LGFI, McGKFCM, and the SalCor models. The results show that the CV model accurately segmented images with uniform intensity backgrounds but fell short in capturing the ROI when the image had nonuniform intensity in the foreground and/or background. The LBF, VLSBCS, LSACM, and McGKFCM models obtained precise segmentation on images with uniform and nonuniform intensity backgrounds but encountered difficulties in segmenting the ROI of some images with nonuniform intensity foregrounds. The LGFI segmentation results were unsatisfactory, as indicated in Row 6. However, the SalCor model (Row 8) provided the most prominent segmentations on both image types.

Table 3 lists the number of iterations needed for contour to converge and the runtime (final convergence) for all synthetic and real images in Fig. 6 to evaluate the computational performance of the SalCor and SOTA models. The results show that the SalCor model exhibited faster convergence and required fewer iterations for image segmentation than the SOTA models. Although McGKFCM has similar computational efficiency to the proposed SalCor model, it fails to accurately segment all images.

In Fig. 7, the segmentation performance is demonstrated on various medical images, such as real brain MRIs (Row 1), COVID-19 CTs (Row 2), and mammograms (Row 3). The results indicate that the LSACM, VLSBCS, McGKFCM, and LGFI could identify ROI edges but generated inaccurate contours. The CV and LBF contours were dispersed over the area. The brain MRI in Row 1 was segmented more effectively by the LGFI and VLSBCS models in comparison to the other SOTA models, which is evident from the visual outcomes. However, for the COVID-19 CT and mammogram in Row 2 and Row 3 respectively, these models were not successful in producing accurate segmentation. The McGKFCM model achieved excellent segmentation for mammograms and COVID-19 CT. However, Fig. 7 demonstrates that none of the existing SOTA models could produce better segmentation than the SalCor model.

IV. QUALITATIVE AND QUANTITATIVE ANALYSIS

This section comprehensively evaluates the SalCor model on five datasets: brain MRI [40], COVID-CT [41], brain tumor segmentation (BraTS) 2019 [42], mini-MIAS [39], and THUS10000 [43]. The brain MRI dataset consists of 98 MRIs, the BraTS 2019 dataset includes 335 MRIs, the COVID-CT dataset comprises 349 CT images from 216 COVID-19 patients, the mini-MIAS dataset consists of 322 mammogram images, and the THUS10000 dataset encompasses 10,000 real images. Qualitative and quantitative analyses were performed on these datasets to evaluate the performance of the SalCor model. Furthermore, the segmentation results obtained by the SalCor model were compared with those achieved by SOTA models.

Fig. 8, Fig. 9, Fig. 10, and Fig. 11 respectively display segmentation results of brain MRIs from [40], lung CTs from [41], brain MRIs from [42], and mammogram images from [39] with severe nonuniform intensity and noise to demonstrate that the SalCor model is reliable for

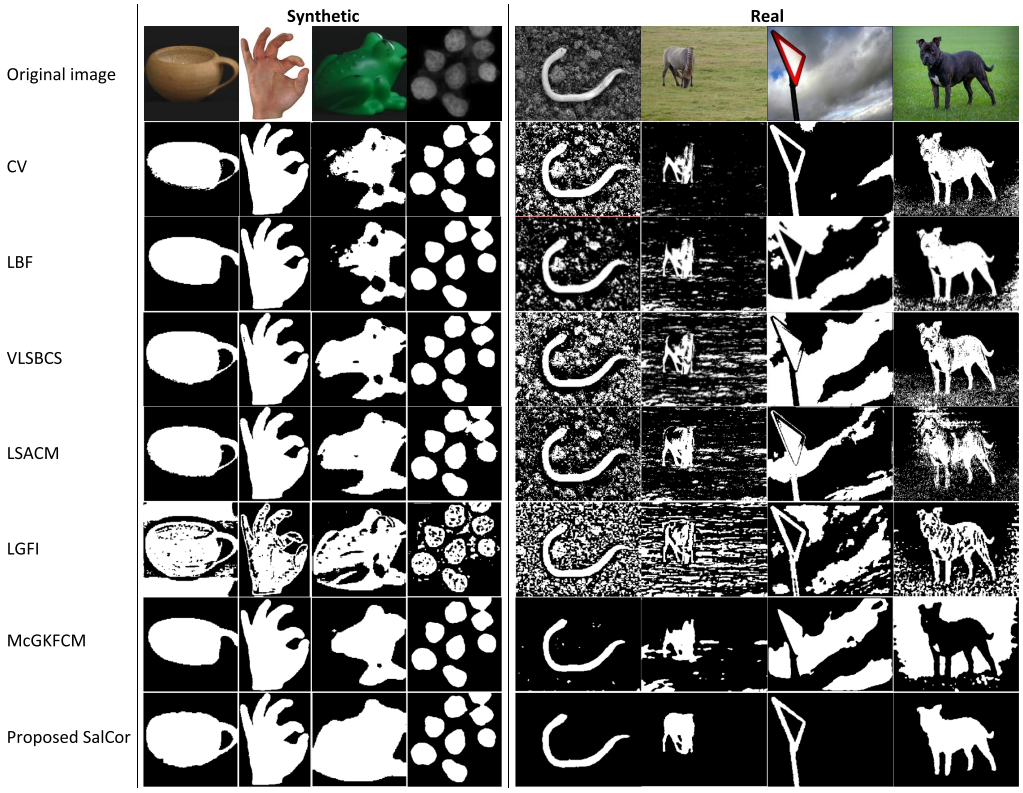

FIGURE 6. Segmentation and corresponding comparison of synthetic and Real images.

TABLE 3. Comparison of number of iterations and runtime for the images in Fig. 6.

Model		Image #1	Image #2	Image #3	Image #4	Image #5	Image #6	Image #7	Image #8
CV	Iteration	500	200	80	200	80	200	20	100
	Runtime	9.43	2.39	2.077	2.427	2.921	20.164	1.94	6.503
LBF	Iteration	50	20	15	20	60	50	20	30
	Runtime	7.2	3.707	2.801	3.198	3.54	6.68	1.71	2.627
VLSBCS	Iteration	10	50	10	50	40	20	20	20
	Runtime	2.01	6.76	1.36	5.15	17.8	28.133	13.95	16.226
LSACM	Iteration	20	20	40	20	40	20	20	20
	Runtime	257.1	34.77	78.77	32.61	238.55	405.97	143.79	160.879
LGFI	Iteration	180	100	100	100	250	190	50	50
	Runtime	9.19	5.053	5.437	4.826	12.34	9.367	2.723	3.347
McGKFCM	Iteration	15	5	25	15	20	30	30	20
	Runtime	0.81	0.301	1.27	1.348	2.231	2.775	2.652	2.663
Proposed SalCor	Iteration	**10**	**5**	**12**	**15**	**15**	**15**	**15**	**15**
	Runtime	**0.43**	**0.283**	**0.701**	**0.673**	**1.872**	**1.923**	**1.482**	**1.957**

medical images. The segmentation results of three brain MRIs from [40] is shown in Fig. 8. The CV model segmentation results are shown in Fig. 8(a), showing inaccurate boundaries in the local region. Similarly, other models failed to produce precise segmentation results due to the presence of nonuniform intensity and noise. Some segmentation results showed undesired contour remains in the background. The LGFI model segmented the global region smoothly, but its segmentation in the local region was inaccurate in presence of nonuniform intensity and noise, as shown in Fig. 8(e). In contrast, the SalCor model incorporates saliency information and consistently produced precise segmentation results irrespective of the nonuniform intensity, as shown in Fig. 8(g).

TABLE 4. Average Metric Analysis of brain MRI dataset [40].

	Accuracy	Sensitivity	Specificity	DSC
CV	0.63	0.68	0.71	0.49
LBF	0.81	0.78	0.72	0.70
VLSBCS	0.83	0.79	0.85	0.81
LSACM	0.66	0.70	0.68	0.50
LGFI	0.9	0.84	0.87	0.89
McGKFCM	0.8	0.78	0.81	0.73
Proposed SalCor	**0.98**	**0.97**	**0.98**	**0.94**

The segmentation results of three CT images from COVID-CT dataset [41] in Fig. 9 are also presented. The images indicate that most lesions are near the dorsal lung

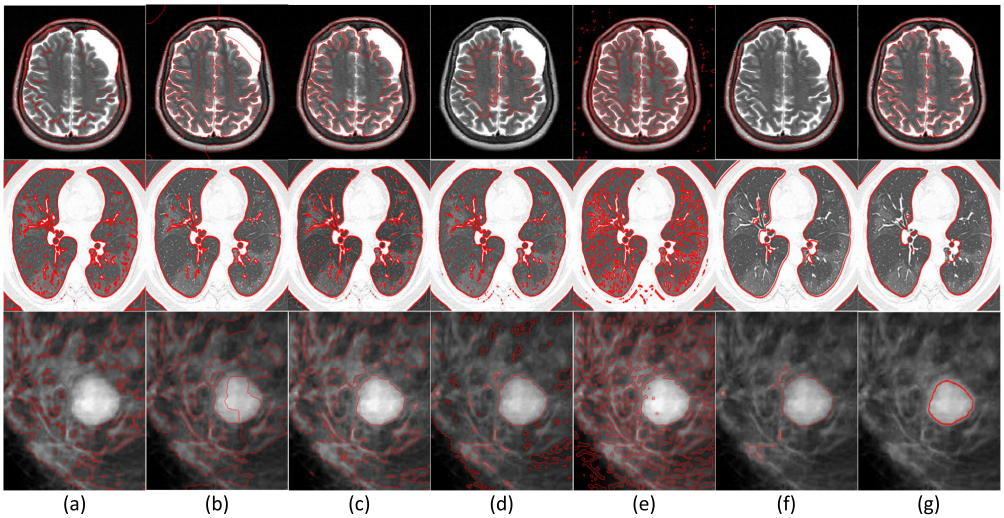

FIGURE 7. Segmentation and corresponding comparison of brain MRI (Row 1), COVID-19 patient's lung CT (Row 2), and mammogram (Row 3). (a) CV, (b) LBF (c) VLSBCS, (d) LSACM, (e) LGFI, (f) McGKFCM, and (g) Proposed SalCor.

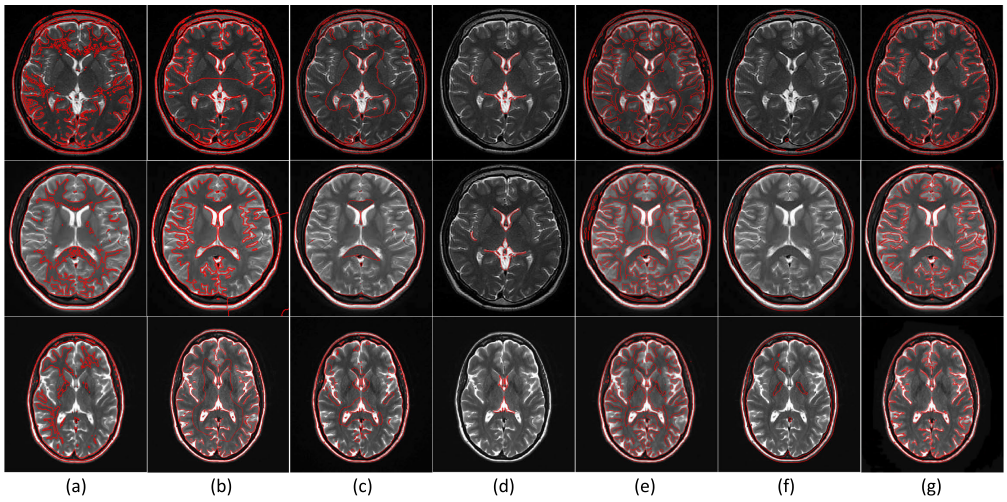

FIGURE 8. Segmentation and comparison of Brain MRIs from [40]. (a) CV, (b) LBF (c) VLSBCS, (d) LSACM, (e) LGFI, (f) McGKFCM, and (g) Proposed SalCor.

TABLE 5. Average Metric Analysis of COVID-CT dataset [41].

	Accuracy	Sensitivity	Specificity	DSC
CV	0.62	0.71	0.69	0.5
LBF	0.8	0.75	0.71	0.74
VLSBCS	0.82	0.79	0.85	0.81
LSACM	0.63	0.69	0.67	0.45
LGFI	0.82	0.83	0.84	0.81
McGKFCM	0.78	0.73	0.70	0.72
Proposed SalCor	**0.98**	**0.97**	**0.98**	**0.95**

region, and it is challenging to differentiate the infected regional boundaries from the chest wall due to its distinct structure and visual features. Thus, past and SOTA segmentation models could not accurately segment the COVID-19 infected region, as shown in Fig. 9(a)-(f). Nonetheless, by utilizing saliency information, the SalCor model could precisely segment the infected areas by detecting the edges of the lungs from challenging backgrounds and contrast implicitly. The results closely resemble manual segmentation, making SalCor a promising approach for early COVID-19 screening and brain tumor detection. The segmentation accuracy of the SalCor model outperforms the SOTA models, as shown in Fig. 9(g).

Fig. 10 and Fig. 11 illustrate the segmentation results for three MRIs from the BraTS 2019 dataset [42] and three mammograms from mini-MIAS dataset [39], respectively. Fig. 10(a) and Fig. 11(a) present the ground truths, which serve as a reference for evaluating the accuracy of the segmentation methods. Fig. 10(b)-(e) and Fig. 11(b)-(e) represent the results obtained using LBF, VLSBCS, LSACM, and the proposed SalCor model, respectively. In Fig. 10, the SalCor model outperforms other models by accurately capturing tumor regions in the brain MRIs from the BraTS 2019 dataset [42]. Similarly, in Fig. 11, the SalCor model

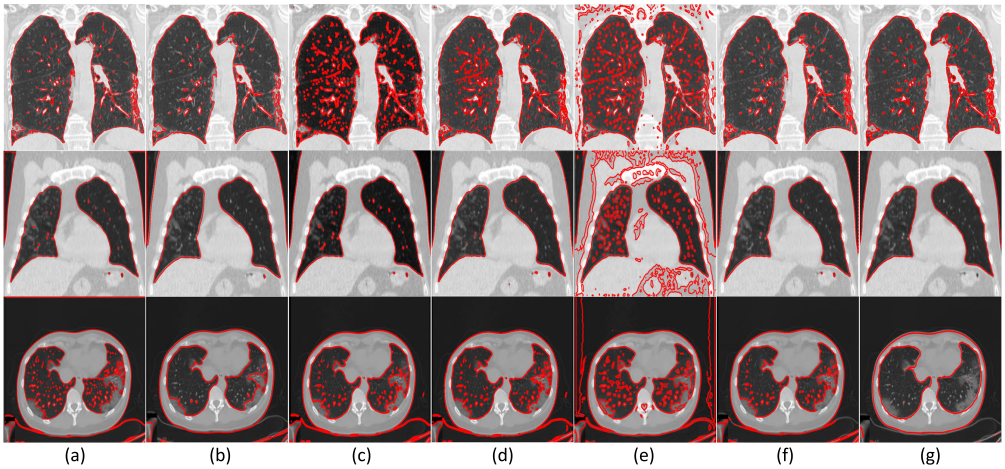

FIGURE 9. Segmentation and comparison of COVID-19 patient's lung CT from [41]. (a) CV, (b) LBF (c) VLSBCS, (d) LSACM, (e) LGFI, (f) McGKFCM, and (g) Proposed SalCor.

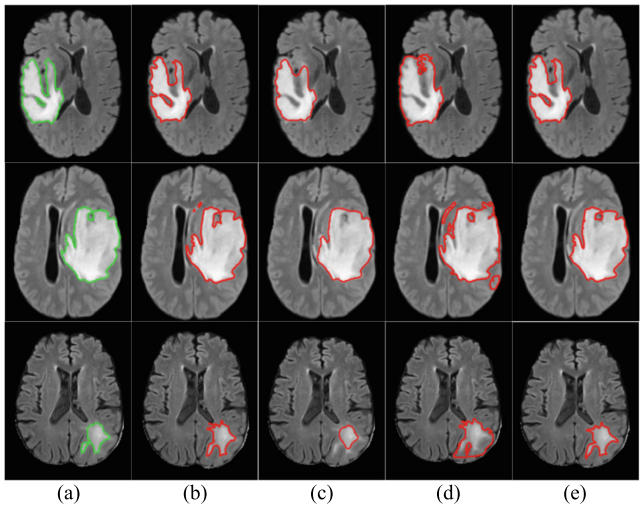

FIGURE 10. Segmentation and comparison of brain MRIs from [42]. (a) Ground Truth (b) LBF (c) VLSBCS, (d) LSACM, and (e) Proposed SalCor.

TABLE 6. Average Metric Analysis of BraTS 2019 dataset [42].

	Accuracy	Sensitivity	Specificity	DSC
LBF	0.841	0.827	0.801	0.771
VLSBCS	0.869	0.854	0.795	0.783
LSACM	0.735	0.704	0.695	0.594
Proposed SalCor	**0.973**	**0.949**	**0.941**	**0.927**

demonstrates its effectiveness by accurately segmenting ROI in the mammogram images from [39]. These results highlight the robustness and superior performance of the SalCor model in handling different medical imaging datasets and achieving precise segmentation outcomes.

The quantitative analysis of the SalCor model was conducted using various metrics, including accuracy, sensitivity, specificity, and Dice similarity coefficient (DSC). Table 4, Table 5, Table 6, and Table 7 present the results obtained of applying the models to the brain MRI [40], COVID-CT [41],

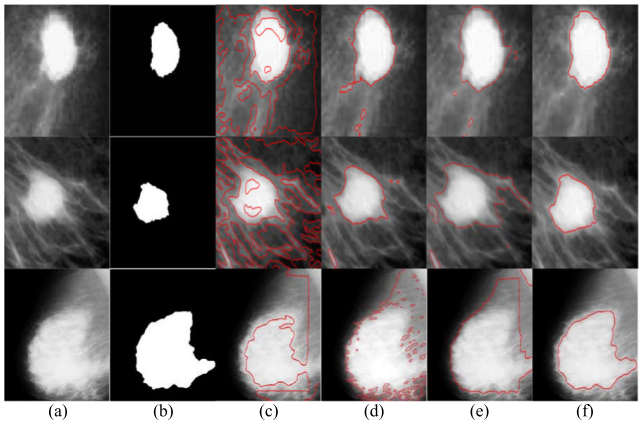

FIGURE 11. Segmentation and comparison of mammogram images from [39]. (a) Original image (b) Ground Truth (c) LBF (d) VLSBCS, (e) LSACM, and (f) Proposed SalCor.

BraTS 2019 [42], and mini-MIAS [39] datasets, respectively. In the context of region segmentation, the following metrics are commonly used to evaluate model performance: accuracy, measuring the correlation between the actual and segmented regions; sensitivity, describing the ability to detect the ROI; specificity, measuring the capability to disregard irrelevant regions; and DSC, quantifying the coherence between the actual and segmented regions. They are defined as [30]

$$\text{Accuracy} = \frac{\text{TP} + \text{TN}}{\text{TP} + \text{TN} + \text{FP} + \text{FN}}, \tag{28}$$

$$\text{Sensitivity} = \frac{\text{TP}}{\text{TP} + \text{FN}}, \tag{29}$$

$$\text{Specificity} = \frac{\text{TN}}{\text{TN} + \text{FP}}, \tag{30}$$

$$\text{DSC} = \frac{2\text{TP}}{2\text{TP} + \text{FP} + \text{FN}}. \tag{31}$$

In evaluating segmentation models, values closer to 1 are generally deemed acceptable. The true positive (TP) and

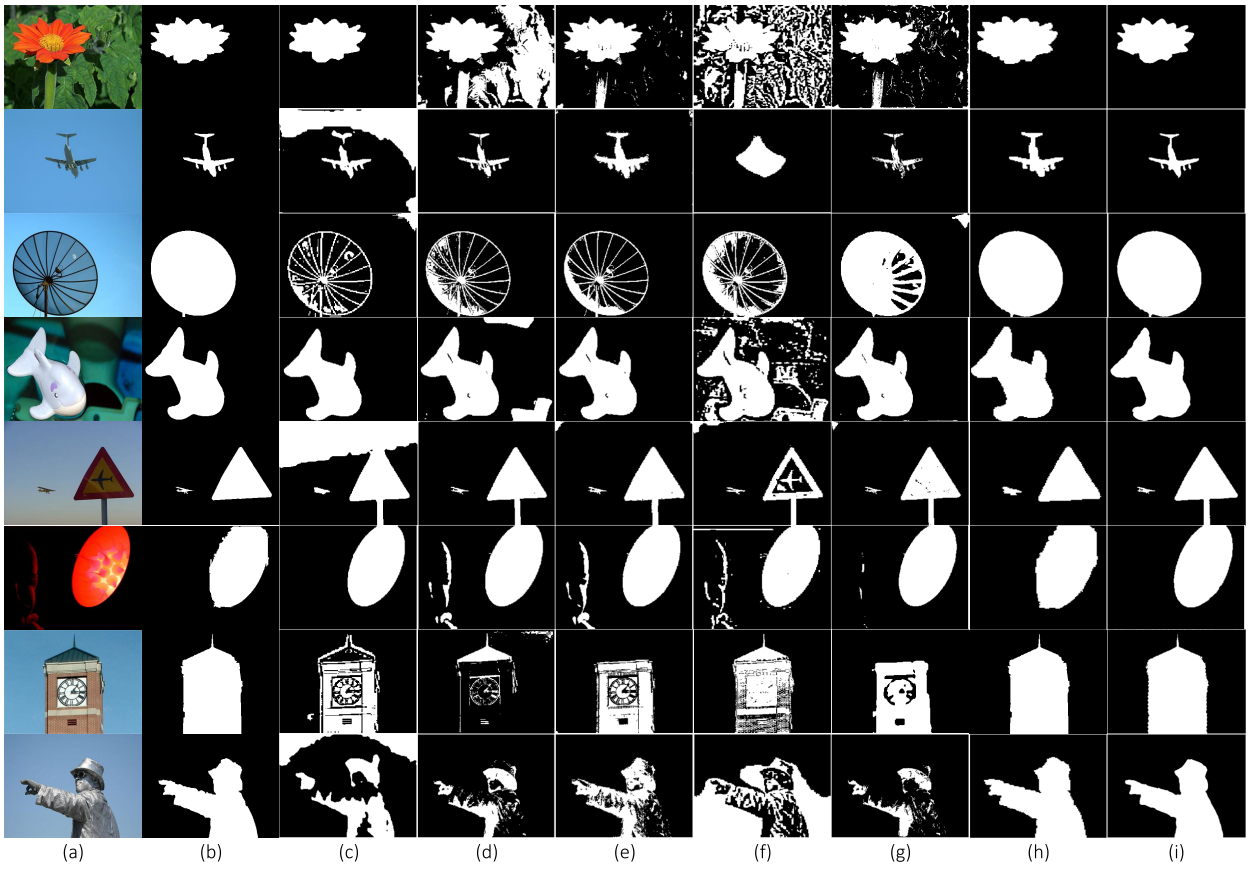

FIGURE 12. Real image segmentation and comparison from [43]. (a) Original image, (b) Ground truth, (c) LBF, (d) VLSBCS, (e) LSACM, (f) LGFI, (g) McGKFCM, (h) DRU, and (i) Proposed SalCor.

TABLE 7. Average Metric Analysis of mini-MIAS dataset [39].

	Accuracy	Sensitivity	Specificity	DSC
LBF	0.852	0.791	0.783	0.788
VLSBCS	0.921	0.796	0.795	0.891
LSACM	0.943	0.921	0.892	0.945
Proposed SalCor	**0.984**	**0.971**	**0.965**	**0.979**

TABLE 8. Average Metric Analysis of THUS10000 dataset [43].

	Accuracy	Sensitivity	Specificity	DSC
LBF	0.871	0.836	0.783	0.574
VLSBCS	0.826	0.822	0.795	0.541
LSACM	0.761	0.693	0.739	0.548
LGFI	0.705	0.832	0.740	0.286
McGKFCM	0.837	0.828	0.808	0.581
DRU	0.923	0.851	0.886	0.681
Proposed SalCor	**0.979**	**0.937**	**0.971**	**0.854**

true negative (TN) indicate the accurately segmented and unsegmented regions, whereas the false positive (FP) and false negative (FN) signify the falsely detected and undetected regions, respectively. Table 4, Table 5, Table 6, and Table 7 reveal that the SalCor model outperformed previous models for accuracy, sensitivity, specificity, and DCS on brain MRI [40], COVID-CT [41], BraTS 2019 [42], and mini-MIAS [39] datasets, respectively.

In addition, the THUS10000 dataset [43], consisting of 10,000 real images, was also used to test the performance metrics obtained by the SalCor model in the context of qualitative and quantitative analysis. The segmentation results obtained by the SalCor model on eight images from [43] are shown and compared with the SOTA models in Fig. 12. The average accuracy, sensitivity, specificity, and DSC for SalCor and other comparative models are shown in Table 8. To obtain the average performance metrics, 300 images from 10000 images in THUS10000 dataset are selected randomly and segmentation is performed. According to Fig. 12 and Table 8, the proposed SalCor model yielded the best segmentation results for real images in [43].

Furthermore, [43] was employed to evaluate the precision and recall of the SalCor and previous models. Precision is calculated as $P = \frac{|R_S \cap R_{GT}|}{|R_S|}$ and Recall is calculated as $R = \frac{|R_S \cap R_{GT}|}{|R_{GT}|}$. The PR curve of all models, including a Dual-gated Recurrent UNet (DRU) [44], were plotted and compared in Fig. 13. The DRU was trained using 20% of the THUS10000 dataset, 20% was used for validation, and the remaining 60% for testing. The model was trained with the VGG-16 optimizer with batch size 8 and 250 $\times$ 250 sized patches for 100 epochs. The rate of learning was set to 6×10^{-4}.

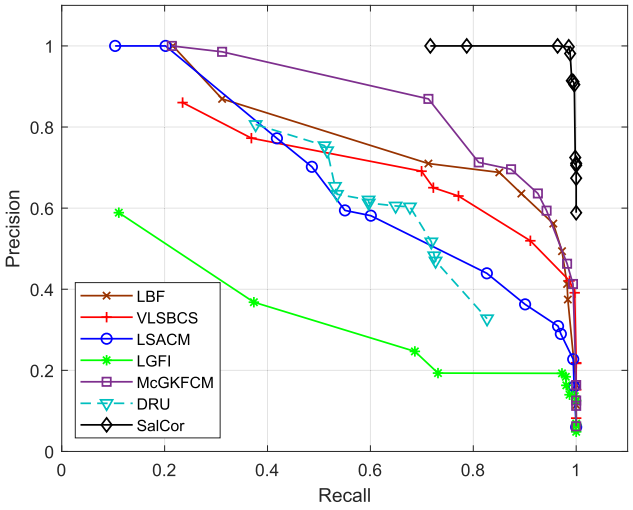

FIGURE 13. PR curve from segmentation of images in [43].

The results indicate that the SalCor model outperforms DRU regarding performance metrics. This could be due to overfitting, which occurs when a model performs well on the training data but poorly on new data, especially on a small dataset like THUS10000.

V. DISCUSSION

The SalCor model offers several advantages not only for medical image segmentation but also for natural images. Firstly, it effectively addresses the challenge of intensity inhomogeneity commonly present in medical images, ensuring accurate and robust segmentation results. By incorporating saliency information, the SalCor model can detect and emphasize relevant image features, improving the delineation of ROI. Secondly, the SalCor model provides explicit control over the contour evolution process, allowing users to guide and refine the segmentation according to their specific requirements. This interactive nature enables experts to incorporate their domain knowledge and fine-tune the segmentation results. Additionally, the SalCor model benefits from a solid theoretical foundation in ACMs, making it well-understood and enabling further advancements and extensions tailored to specific segmentation tasks. Overall, the SalCor model offers a powerful and reliable approach to medical image segmentation, addressing key challenges and providing valuable control and adaptability for accurate results. However, it may have limited representation power, require manual feature engineering, and be sensitive to parameter tuning.

On the other hand, deep learning models like DRU excel in learning hierarchical representations, achieving SOTA performance, and handling large-scale datasets. They eliminate the need for manual feature engineering and can adapt well to diverse data. However, they require large amounts of annotated data, have computational complexity, and lack interpretability. These advantages and disadvantages highlight the trade-offs between ACMs like the SalCor model and deep learning models, emphasizing the importance of selecting the appropriate approach based on specific requirements and constraints.

VI. CONCLUSION

In this study, a novel SalCor model was proposed, which incorporates saliency information with local correntropy-based K-means clustering as an energy function, enabling it to effectively extract objects with complex backgrounds regardless of noise and nonuniform intensity. An adaptive weight function is incorporated in the energy function to improve the model resilience to contour initialization and improve robustness. The SalCor model can handle noise robustly by leveraging the LCE and employs the RSD instead of the SGD for faster convergence and lower runtime. The SalCor model was evaluated on synthetic, real, and medical images with varying intensity variations. Several SOTA models were compared with regards to their number of iterations and runtime. The qualitative and quantitative analyses were conducted on the brain MRI, COVID-CT, BraTS 2019, mini-MIAS, and THUS10000 datasets using accuracy, sensitivity, specificity, and DCS. The performance evaluation of the SalCor model on brain MRI and COVID-CT datasets revealed that it outperforms all conventional ACMs with accuracy improvements of (55%, 21%, 18%, 48.5%, 8.88%, and 22.5%) and (58%, 22.5%, 19.5%, 55%, 19.5%, and 25.64%), respectively, for the following methods: CV, LBF, VLSBCS, LSACM, LGFI, and McGKFCM. In additon, the performance evaluation on BraTS 2019 and mini-MIAS datasets show better accuracy by (14.5%, 11.29%, and 27.87%) and (14.38%, 6.61%, and 4.25%) than LBF, VLSBCS, and LSACM, respectively. Moreover, the superiority of the SalCor was also reflected in its runtime, which was significantly reduced compared to the SOTA models. Similarly, the SalCor model outperforms previous ACMs and the DRU in terms of the precision, recall, and other performance metrics for THUS10000 dataset.

REFERENCES

[1] D. A. Forsyth and J. Ponce, *Computer Vision: A Modern Approach*, 2nd ed. London, U.K.: Pearson, 2012.
[2] A. Tiwari, S. Srivastava, and M. Pant, "Brain tumor segmentation and classification from magnetic resonance images: Review of selected methods from 2014 to 2019," *Pattern Recognit. Lett.*, vol. 131, pp. 244–260, Mar. 2020.
[3] M. Kass, A. Witkin, and D. Terzopoulos, "Snakes: Active contour models," *Int. J. Comput. Vis.*, vol. 1, no. 4, pp. 321–331, Jan. 1988.
[4] V. Caselles, R. Kimmel, and G. Sapiro, "Geodesic active contours," *Int. J. Comput. Vis.*, vol. 22, no. 1, pp. 61–79, 1997.
[5] C. Li, C. Xu, C. Gui, and M. D. Fox, "Level set evolution without re-initialization: A new variational formulation," in *Proc. IEEE Comput. Soc. Conf. Comput. Vis. Pattern Recognit. (CVPR)*, Jun. 2005, pp. 430–436.
[6] C. Li, C. Xu, C. Gui, and M. D. Fox, "Distance regularized level set evolution and its application to image segmentation," *IEEE Trans. Image Process.*, vol. 19, no. 12, pp. 3243–3254, Dec. 2010.
[7] H. Yu, F. He, and Y. Pan, "A novel segmentation model for medical images with intensity inhomogeneity based on adaptive perturbation," *Multimedia Tools Appl.*, vol. 78, no. 9, pp. 11779–11798, May 2019.
[8] D. Mumford and J. Shah, "Optimal approximations by piecewise smooth functions and associated variational problems," *Commun. Pure Appl. Math.*, vol. 42, no. 5, pp. 577–685, Jul. 1989.

[9] T. F. Chan and L. A. Vese, "Active contours without edges," *IEEE Trans. Image Process.*, vol. 10, no. 2, pp. 266–277, Feb. 2001.

[10] C. Li, C.-Y. Kao, J. C. Gore, and Z. Ding, "Minimization of region-scalable fitting energy for image segmentation," *IEEE Trans. Image Process.*, vol. 17, no. 10, pp. 1940–1949, Oct. 2008.

[11] C. Li, R. Huang, Z. Ding, C. Gatenby, D. Metaxas, and J. Gorel, "A variational level set approach to segmentation and bias correction of images with intensity inhomogeneity," in *Proc. Int. Conf. Med. Image Comput. Comput.-Assist. Intervent.*, vol. 11, no. 2, Nov. 2008, pp. 1083–1091.

[12] K. Zhang, L. Zhang, H. Song, and W. Zhou, "Active contours with selective local or global segmentation: A new formulation and level set method," *Image Vis. Comput.*, vol. 28, no. 4, pp. 668–676, Apr. 2010.

[13] L. Wang and C. Pan, "Robust level set image segmentation via a local correntropy-based K-means clustering," *Pattern Recognit.*, vol. 47, no. 5, pp. 1917–1925, May 2014.

[14] K. Zhang, L. Zhang, K.-M. Lam, and D. Zhang, "A level set approach to image segmentation with intensity inhomogeneity," *IEEE Trans. Cybern.*, vol. 46, no. 2, pp. 546–557, Feb. 2016.

[15] S. Soomro, T. A. Soomro, and K. N. Choi, "An active contour model based on region based fitting terms driven by p-Laplace length regularization," *IEEE Access*, vol. 6, pp. 58272–58283, 2018.

[16] A. Munir, S. Soomro, M. T. Shahid, T. A. Soomro, and K. N. Choi, "Hybrid active contours driven by edge and region fitting energies based on p-Laplace equation," *IEEE Access*, vol. 7, pp. 135399–135412, 2019.

[17] J. Fang, H. Liu, L. Zhang, J. Liu, and H. Liu, "Fuzzy region-based active contours driven by weighting global and local fitting energy," *IEEE Access*, vol. 7, pp. 184518–184536, 2019.

[18] A. Niaz, K. Rana, A. Joshi, A. Munir, D. D. Kim, H. C. Song, and K. N. Choi, "Hybrid active contour based on local and global statistics parameterized by weight coefficients for inhomogeneous image segmentation," *IEEE Access*, vol. 8, pp. 57348–57362, 2020.

[19] W. Zhang, X. Wang, J. Chen, and W. You, "A new hybrid level set approach," *IEEE Trans. Image Process.*, vol. 29, pp. 7032–7044, 2020.

[20] A. Joshi, M. S. Khan, A. Niaz, F. Akram, H. C. Song, and K. N. Choi, "Active contour model with adaptive weighted function for robust image segmentation under biased conditions," *Expert Syst. Appl.*, vol. 175, Aug. 2021, Art. no. 114811.

[21] A. Elnakib, G. Gimel'farb, J. S. Suri, and A. El-Baz, "Medical image segmentation: A brief survey," in *Multi Modality State-of-the-Art Medical Image Segmentation and Registration Methodologies*. New York, NY, USA: Springer, 2011, pp. 1–39.

[22] A.-R. Ali, M. Couceiro, A. Anter, and A.-E. Hassanien, "Particle swarm optimization based fast fuzzy C-means clustering for liver CT segmentation," in *Applications of Intelligent Optimization in Biology and Medicine: Current Trends and Open Problems*, A.-E. Hassanien, C. Grosan, and M. Fahmy Tolba, Eds. Cham, Switzerland: Springer, 2016, pp. 233–250.

[23] A. M. Foust, G. S. Phillips, W. C. Chu, P. Daltro, K. M. Das, P. Garcia-Peña, T. Kilborn, A. J. Winant, and E. Y. Lee, "International expert consensus statement on chest imaging in pediatric COVID-19 patient management: Imaging findings, imaging study reporting, and imaging study recommendations," *Radiol., Cardiothoracic Imag.*, vol. 2, no. 2, Apr. 2020, Art. no. e200214.

[24] L. O. Hall, A. M. Bensaid, L. P. Clarke, R. P. Velthuizen, M. S. Silbiger, and J. C. Bezdek, "A comparison of neural network and fuzzy clustering techniques in segmenting magnetic resonance images of the brain," *IEEE Trans. Neural Netw.*, vol. 3, no. 5, pp. 672–682, Sep. 1992.

[25] D.-P. Fan, T. Zhou, G.-P. Ji, Y. Zhou, G. Chen, H. Fu, J. Shen, and L. Shao, "Inf-Net: Automatic COVID-19 lung infection segmentation from CT images," *IEEE Trans. Med. Imag.*, vol. 39, no. 8, pp. 2626–2637, Aug. 2020.

[26] H. Li and K. N. Ngan, "Saliency model-based face segmentation and tracking in head-and-shoulder video sequences," *J. Vis. Commun. Image Represent.*, vol. 19, no. 5, pp. 320–333, Jul. 2008.

[27] X. Bai and W. Wang, "Saliency-SVM: An automatic approach for image segmentation," *Neurocomputing*, vol. 136, pp. 243–255, Jul. 2014.

[28] C. Qin, G. Zhang, Y. Zhou, W. Tao, and Z. Cao, "Integration of the saliency-based seed extraction and random walks for image segmentation," *Neurocomputing*, vol. 129, pp. 378–391, Apr. 2014.

[29] L. Yang, D. Xin, L. Zhai, F. Yuan, and X. Li, "Active contours driven by visual saliency fitting energy for image segmentation in SAR images," in *Proc. IEEE 4th Int. Conf. Cloud Comput. Big Data Anal. (ICCCBDA)*, Apr. 2019, pp. 393–397.

[30] A. Joshi, M. S. Khan, S. Soomro, A. Niaz, B. S. Han, and K. N. Choi, "SRIS: Saliency-based region detection and image segmentation of COVID-19 infected cases," *IEEE Access*, vol. 8, pp. 190487–190503, 2020.

[31] R. Achanta, S. Hemami, F. Estrada, and S. Susstrunk, "Frequency-tuned salient region detection," in *Proc. IEEE Conf. Comput. Vis. Pattern Recognit.*, Jun. 2009, pp. 1597–1604.

[32] F. Lecellier, S. Jehan-Besson, J. Fadili, G. Aubert, and M. Revenu, "Optimization of divergences within the exponential family for image segmentation," in *Scale Space and Variational Methods in Computer Vision*. Berlin, Germany: Springer, 2009, pp. 137–149.

[33] S. Amari and S. C. Douglas, "Why natural gradient?" in *Proc. IEEE Int. Conf. Acoust., Speech Signal Process. (ICASSP)*, May 1998, pp. 1213–1216.

[34] F. Nielsen and R. Nock, "Entropies and cross-entropies of exponential families," in *Proc. IEEE Int. Conf. Image Process.*, Sep. 2010, pp. 3621–3624.

[35] F. Lecellier, J. Fadili, S. Jehan-Besson, G. Aubert, M. Revenu, and E. Saloux, "Region-based active contours with exponential family observations," *J. Math. Imag. Vis.*, vol. 36, no. 1, pp. 28–45, Jan. 2010.

[36] S. Amari, *Differential-Geometrical Methods in Statistics*. New York, NY, USA: Springer-Verlag, 1990.

[37] F. Akram, M. A. Garcia, and D. Puig, "Active contours driven by local and global fitted image models for image segmentation robust to intensity inhomogeneity," *PLoS ONE*, vol. 12, no. 4, Apr. 2017, Art. no. e0174813, doi: 10.1371/journal.pone.0174813.

[38] L. Panigrahi, K. Verma, and B. K. Singh, "Ultrasound image segmentation using a novel multi-scale Gaussian kernel fuzzy clustering and multi-scale vector field convolution," *Expert Syst. Appl.*, vol. 115, pp. 486–498, Jan. 2019.

[39] J. Suckling, "The mammographic image analysis society digital mammogram database," in *Exerpta Medica: International Congress Series*, vol. 1069. Amsterdam, The Netherlands: Elsevier, 1994, pp. 375–378.

[40] N. Chakrabarty. (2019). *Brain MRI Images for Brain Tumor Detection*. [Online]. Available: https://www.kaggle.com/navoneel/brain-mri-images-for-brain-tumor-detection

[41] X. Yang, X. He, J. Zhao, Y. Zhang, S. Zhang, and P. Xie, "COVID-CT-dataset: A CT scan dataset about COVID-19," 2020, *arXiv:2003.13865*.

[42] B. H. Menze, "The multimodal brain tumor image segmentation benchmark (BRATS)," *IEEE Trans. Med. Imag.*, vol. 34, no. 10, pp. 1993–2024, Oct. 2015.

[43] M.-M. Cheng, N. J. Mitra, X. Huang, P. H. S. Torr, and S.-M. Hu, "Global contrast based salient region detection," *IEEE Trans. Pattern Anal. Mach. Intell.*, vol. 37, no. 3, pp. 569–582, Mar. 2015.

[44] W. Wang, K. Yu, J. Hugonot, P. Fua, and M. Salzmann, "Recurrent U-Net for resource-constrained segmentation," in *Proc. IEEE/CVF Int. Conf. Comput. Vis. (ICCV)*, Oct. 2019, pp. 2142–2151.

ADITI JOSHI received the B.S. degree in computer science and the M.B.A. degree in marketing from Mumbai University, India, in 2014 and 2016, respectively, and the M.S. degree in computer science and engineering from Chung-Ang University, Seoul, South Korea, in 2021, where she is currently pursuing the Ph.D. degree with the Department of Computer Science and Engineering.

Since 2019, she has been a Research Assistant with the Visual Image Media Laboratory, Chung-Ang University. Her current research interests include medical image analysis, semantic segmentation, face and gesture recognition, and machine learning.

MOHAMMED SAQUIB KHAN (Member, IEEE) received the B.E. degree in electronics and telecommunication engineering from Mumbai University, Mumbai, India, in 2015, and the Ph.D. degree in electrical and electronics engineering with a major in communication and signal processing from Chung-Ang University, Seoul, South Korea, in 2020.

During the Ph.D. degree, he was a Research Assistant with the Mobile Communications Laboratory, Chung-Ang University, where he continued as a Postdoctoral Fellow, in 2021. He is currently a Chief Engineer with the Samsung Research and Development Institute, Bengaluru, India. He is the author of more than 30 international conferences and articles. His research interests include wireless communication systems, digital signal processing, image processing, and machine learning.

Dr. Khan was a member of the Korea Institute of Communications and Information Sciences. He was a recipient of the Chung-Ang University Young Scientist Scholarship (CAYSS) for the M.S. and Ph.D. degrees; the Samsung HumanTech Paper Encouragement Award, in 2020; the Samsung Excellence Super Tech Award, in 2022; and the Samsung Team Awesome Award, in 2022.

JIN KIM received the B.S. and M.S. degrees in computer science and engineering from Chung-Ang University, Seoul, South Korea, in 2014 and 2016, respectively.

He is currently a Lead Software Engineer with SecuLayer Inc., Seoul. His research interests include auto machine learning, artificial intelligence, and bigdata AI platform.

KWANG NAM CHOI received the B.S. and M.S. degrees from the Department of Computer Science, Chung-Ang University, Seoul, South Korea, in 1988 and 1990, respectively, and the Ph.D. degree in computer science from the University of York, U.K., in 2002.

He is currently a Professor with the School of Computer Science and Engineering, Chung-Ang University. His current research interests include motion tracking, object categorization, and 3D image recognition.